Defluorination/fluorination mechanism of $Bi_{0.8}Ba_{0.2}F_{2.8}$ as a fluoride shuttle battery positive electrode

Keiji Shimoda[a,*], Taketoshi Minato[b,*], Hiroaki Konishi[a,*], Gentaro Kano[a], Tomotaka Nakatani[a], So Fujinami[a], Asuman Celik Kucuk[b], Shogo Kawaguchi[c], Zempachi Ogumi[a], Takeshi Abe[d]

[a] *Office of Society-Academia Collaboration for Innovation, Kyoto University, Gokasho, Uji, Kyoto 611-0011, Japan*

[b] *Office of Society-Academia Collaboration for Innovation, Kyoto University, Katsura, Nishikyo, Kyoto 615-8530, Japan*

[c] *Japan Synchrotron Radiation Research Institute (JASRI), Kouto 1-1, Sayo, Hyogo 679-5198, Japan*

[d] *Gradual School of Global Environmental Studies, Kyoto University, Katsura, Nishikyo, Kyoto 615-8510, Japan*

Abstract

Fluoride shuttle batteries (FSBs), which utilize F^- ion migration in electrochemical reactions, have recently advanced in academic research as next-generation rechargeable batteries. Bismuth trifluoride (BiF_3) and its relatives are expected to be promising positive electrode materials for FSBs because of their high theoretical capacity. Herein, the defluorination/fluorination reaction of a BaF_2-doped BiF_3, $Bi_{0.8}Ba_{0.2}F_{2.8}$, positive electrode was investigated using synchrotron-radiation X-ray diffraction, X-ray absorption spectroscopy, and transmission electron microscopy. The $Bi_{0.8}Ba_{0.2}F_{2.8}$ electrode showed a higher reversible capacity in the first cycle and improved capacity

retention compared to the BiF_3 electrode. The pristine $Bi_{0.8}Ba_{0.2}F_{2.8}$ showed a tysonite-type structure, and metallic Bi and BaF_2 nanoparticles were observed in the fully defluorinated state. Moreover, we found that the (re-)fluorinated material consisted of BiF_3 and BaF_2 nanoparticles, indicating that bismuth is the only redox active element, and that the tysonite structure is not recovered after the initial discharging. This suggests that the cycle performance of the $Bi_{0.8}Ba_{0.2}F_{2.8}$ electrode may be improved due to the suppression of the coarsening of BiF_3 nanoparticles by the adhesion of BaF_2 nanoparticles formed after initial defluorination.

Keywords:

Fluoride shuttle battery; Bismuth trifluoride; Tysonite

*Corresponding authors:

Keiji Shimoda

Office of Society-Academia Collaboration for Innovation, Kyoto University, Gokasho, Uji 611-0011, Japan

E-mail address: shimoda.keiji.6v@kyoto-u.ac.jp

Tel: +81-774-38-4967, Fax: +81-774-38-4996

Taketoshi Minato

(Present address) Institute for Molecular Science, National Institutes of Natural Sciences, Nishigonaka 38, Myodaiji-cho, Okazaki, Aichi 444-8585, Japan

E-mail address: minato@ims.ac.jp

Tel: +81-564-55-7330

Hiroaki Konishi

(Present address) Research & Development Group, Hitachi Ltd., Omika-cho 1-1, Hitachi, Ibaraki 319-1292, Japan

E-mail address: hiroaki.konishi.yj@hitachi.com

Tel: +81-294-52-5111

1. Introduction

Rechargeable lithium-ion batteries (LIBs) have been successfully used worldwide as a power source for portable devices, such as laptop computers and smartphones. The global market for electric vehicles currently demands highly secure batteries with lower cost and higher energy density. Substantial efforts have been dedicated to the development of next-generation batteries to replace LIBs. In recent years, researches have advanced on fluoride shuttle batteries (FSBs) that utilize F^- ion migration in electrochemical reactions [1–5]. Metal fluorides (MF_x, M = metal) generally show a high F/M ratio and, therefore, exhibit high theoretical capacities based on the following conversion-type reaction:

$MF_x + xe^- \rightarrow M + xF^-$ (discharging process at a positive electrode).

For example, the theoretical capacities of bismuth trifluoride (BiF_3), copper difluoride (CuF_2), and iron trifluoride (FeF_3) are calculated to be 302, 528, and 712 mAh g^{-1}, respectively. A recent theoretical calculation suggested that the defluorination of most metal fluorides proceeds via a two-phase reaction [6].

Fichtner et al. demonstrated all-solid-state FSBs using a solid electrolyte with high F^- ion conductivity [7]. Fluoride solid electrolytes have excellent thermal stability and are stable over a wide potential window; additionally, many candidate materials have been reported [8]. Unfortunately, the F^- ion conductivities of these materials are rather low near room temperature. Room-temperature all-solid-state FSBs using $BaSnF_4$ as solid electrolyte were recently demonstrated [9], but the practical operation of all-solid-state FSBs still requires a high temperature of 150 °C [7,9]. FSBs using liquid electrolytes are expected to allow electrochemical operation at room temperature. Several liquid electrolytes using different fluoride salts and solvents have been proposed in recent years. Okazaki et al. prepared a liquid electrolyte containing an organic fluoride

salt (1-methyl-1-propylpiperidinium fluoride: MPPF) in an ionic liquid (*N*,*N*,*N*-trimethyl-*N*-propylammonium bis(trifluoromethanesulfonyl)amide: TMPA-TFSA) at a molar ratio of 1:50 [10]. A fluorohydrogenate ionic liquid electrolyte ($[C_2C_1im][(FH)_{2.3}F]$, C_2C_1im = 1-ethyl-3-methylimdazolium) showing a high ionic conductivity was also reported for FSBs [11,12]. Davis et al. used a liquid electrolyte of 0.75 M *N*,*N*,*N*-trimetyl-*N*-neopentylammonium fluoride (Np_1F) or *N*,*N*,*N*-dimetyl-*N*,*N*-dineopentylammonium fluoride (Np_2F) in bis(2,2,2-trifluoroethyl)ether (BTFE) [13]. Similarly, by adding an anion acceptor (AA) that improves the solubility of inorganic fluoride salts, such as cesium fluoride (CsF), to an organic solvent, bis[2-(2-methoxyethoxy)ethyl]ether (tetraglyme, G4) or a siloxane-based solvent, 2,2,4,4-tetramethyl-3,8,11,14,17-pentaoxa-2,4-disilaoctadecane, we successfully produced a stable liquid electrolyte suitable for FSBs operating at room temperature [14–18].

BiF_3 reportedly undergoes a defluorination/fluorination (discharge/charge) reaction as a positive electrode material for FSBs. The first discharging profile was shown at 150 °C for the all-solid-state cell composed of $Ce/La_{0.9}Ba_{0.1}F_{2.9}/BiF_3$ [7]. The reported discharging capacity was 126 mAh g^{-1}—much less than the theoretical capacity of 302 mAh g^{-1}. In a recent literature, the all-solid-state cell composed of $Sn/BaSnF_4/BiF_3$ demonstrated the first discharging capacity of 120 mAh g^{-1} at 25 °C and 281 mAh g^{-1} at 150 °C, and rapid capacity deterioration was observed with discharge–charge cycling at 25 °C [9]. Okazaki et al. showed a reversible charge–discharge profile at room temperature for a liquid-based cell comprising PbF_2/MPPF-TMPA-TFSA/Bi [10]. This study also reported rapid capacity deterioration with electrochemical cycling. Observation of the BiF_3 microparticle morphology using in situ micro-Raman spectroscopy showed that the defluorination mechanism could differ depending on the type of electrolyte applied [19–21]: the defluorination reaction under 0.45 M CsF + AA electrolyte solution proceeded according to a dissolution-deposition mechanism (BiF_3 (solid) → Bi^{3+} (solution) → metallic Bi (solid)). However,

a direct defluorination mechanism (BiF_3 (solid) → metallic Bi (solid)) had an increasing contribution when saturated CsF (0.5 M) + AA electrolyte solution was applied. Moreover, the crystal structure of pristine BiF_3 (orthorhombic, o-BiF_3, *Pnma*) changed to cubic or trigonal BiF_3 (c-BiF_3, *Fm*–3*m* or t-BiF_3, *P*–3*c*1, respectively) via defluorination/fluorination reactions depending on the type of electrolyte [19,20]. BiF_3/C composite subjected to high-energy ball milling was recently shown to improve electrochemical performance due to decreased particle size and better mixing with electrically conductive carbon to obtain a discharging capacity close to the theoretical capacity [22]. However, capacity retention with cycling remained poor.

The BiF_3-BaF_2 solid solution ($Bi_{1-x}Ba_xF_{3-x}$) prepared by sintering at 700 °C shows several crystal structures depending on the BaF_2 content [23]. In particular, $Bi_{1-x}Ba_xF_{3-x}$ has a LaF_3 (tysonite)-type structure (trigonal, *P*–3*c*1) when *x* ranges from 0.05–0.17. The tysonite-structured $Bi_{1-x}Ba_xF_{3-x}$ shows high F^- ion conductivities because of F deficiency in the structure introduced by adding a divalent fluoride [23]. Recently, Konishi et al. prepared BaF_2-doped BiF_3 ($Bi_{1-x}Ba_xF_{3-x}$; x = 0, 0.2, and 0.4) by high-energy ball milling and reported that $Bi_{0.8}Ba_{0.2}F_{2.8}$ (x = 0.2) with a tysonite-type structure exhibited good electrochemical performance as an LIB positive electrode [24]. $Bi_{0.8}Ba_{0.2}F_{2.8}$ was subsequently examined as an FSB positive electrode [25]: Ba substitution up to x = 0.2 improved the specific reversible capacity in the first cycle and capacity retention with cycling, whereas its theoretical capacity was reduced compared to that of BiF_3. The Ba atom was found to be redox inactive using X-ray photoelectron spectroscopy (XPS) [25]. Herein, we investigated in detail the defluorination/fluorination mechanism of the $Bi_{0.8}Ba_{0.2}F_{2.8}$ positive electrode using X-ray diffraction (XRD), X-ray pair distribution function (PDF) analyses, X-ray absorption spectroscopy (XAS), and transmission electron microscopy (TEM).

2. Experimental

The experimental procedures follow those of previous studies [22,25]. A BiF_3-BaF_2 solid solution sample, $Bi_{0.8}Ba_{0.2}F_{2.8}$, ($Bi_{1-x}Ba_xF_{3-x}$; $x = 0.2$) was prepared using a mechanical alloying method by mixing an appropriate ratio of BiF_3 (o-BiF_3, Fluorochem) and BaF_2 (Sigma-Aldrich) reagents in a planetary ball mill (Fritsch PULVERISETTE7) at 1100 rpm for 1 h under an Ar atmosphere. The prepared $Bi_{0.8}Ba_{0.2}F_{2.8}$ powder was mixed with carbon (acetylene black, AB) in a planetary ball mill at 1100 rpm for 1 h under an Ar atmosphere to enhance electronic conductivity. The $Bi_{0.8}Ba_{0.2}F_{2.8}$/C composite was mixed with polyvinylidene difluoride (PVDF) binder at a weight ratio of $Bi_{0.8}Ba_{0.2}F_{2.8}$:AB:PVDF = 60:25:15 using *N*-methyl-2-pyrrolidone (NMP). The ball-milled BiF_3/C composite was also prepared in the same manner [22]. A positive electrode was fabricated by pasting the resulting slurry on an Al current collector, which was heated at 110 °C to remove NMP. The electrode loading was ~2.0 mg cm^{-2}. An electrolyte solution contains CsF (Tokyo Chemical Industry) as a supporting electrolyte salt and 2,4,6-triphenylboroxine (TPhBX, Tokyo Chemical Industry) as an AA. The electrolyte solution was prepared as saturated CsF and 0.5 M TPhBX in G4 (Kishida Chemical). The electrode and electrolyte solution were carefully prepared in an Ar-filled glovebox.

The three-electrode electrochemical cell (EC FRONTIER) used for the electrochemical tests consisted of a $Bi_{0.8}Ba_{0.2}F_{2.8}$ positive electrode as the working electrode, a Pt mesh as the counter electrode, and a Ag wire immersed in acetonitrile containing 0.1 M $AgNO_3$ and 0.1 M tetraethylammonium perchlorate (TEAP, 0.587 V vs. standard hydrogen electrode (SHE)) as the reference electrode. The discharge–charge measurements were performed at room temperature in a glovebox using a multichannel potentiostat (VMP-300, BioLogic) with a potential window from –2.0 to –0.2 V (vs. RE) at a current rate of 7.55 mA g^{-1}. The cells were disassembled after electrochemical tests, and the electrode samples were rinsed with G4 and dimethyl carbonate

(DMC) to remove the residual electrolyte.

Synchrotron-radiation XRD (SR-XRD) measurements were performed for powdered samples sealed in 0.3 mm ϕ quartz glass capillaries in the 2θ range of 2.1−78.2° with $\Delta\theta = 0.006°$ at the BL02B2 beamline in SPring-8 (Hyogo, Japan). An incident radiation of 30 keV ($\lambda = 0.4133$ Å) was used and calibrated with the CeO_2 lattice parameters. Pair distribution function (PDF) analyses were performed using the SR-XRD profile data. The X-ray total structure factors, $S(Q)$, were derived from the scattering intensities using the in-house BL04B2 software [26]. The reduced PDFs, $G(r)$, were obtained by the Fourier transform of $S(Q)$ with $Q_{max} = 15.0$ Å^{-1}.

X-ray absorption spectroscopy (XAS) measurements were performed at the BL32B2 beamline in SPring-8. Bi and Ba L_3-edge spectra were obtained in a fluorescent yield mode using a silicon drift detector (SDD, Vortex-EX, SII Nano Technology USA). The photon energy was calibrated using standard Cu foil. The XAS spectra were processed using Athena [27].

Elemental mapping analyses of the electrode samples using electron energy loss spectroscopy (EELS) and energy dispersive X-ray spectrometry (EDS) were performed on a GIF Quantum-ER (Gatan) and a JED-2300T SDD (JEOL), respectively, which were installed on a Cs-corrected scanning transmission electron microscope (Cs-STEM, JEM-ARM200F, JEOL). The powder sample was dispersed by manual grinding in ethanol, and a drop of the suspension was collected on a holey carbon film supported on a copper mesh. All treatments were performed in a vacuum or under an Ar atmosphere. The measurements were performed at ~−150 °C to avoid sample damage during electron beam irradiation (200 kV, 77 μA).

3. Results and Discussion

Figure 1a shows the discharge–charge profiles of the $Bi_{0.8}Ba_{0.2}F_{2.8}$ electrode for three cycles. The

observed initial discharging capacity was 307 mAh g^{-1}, which is greater than the theoretical capacity (260 mAh g^{-1}, assuming that no BaF_2 is involved) due to the side reaction such as electrolyte decomposition [25]. An expanded potential window between –2.0 and –0.2 V resulted in higher discharging and charging capacities than those in the literature [25]. The Coulomb efficiencies of the 1st, 2nd, and 3rd cycles were 85%, 92%, and 93%, respectively, and the 3rd cycle charging capacity was 218 mAh g^{-1}. The discharge–charge profiles of the BiF_3 electrode are shown in Figure S1. The initial discharging capacity of BiF_3 was 330 mAh g^{-1}, but the capacity loss was large: the Coulomb efficiencies of the 1st, 2nd, and 3rd cycles for BiF_3 were 72%, 92%, and 92%, respectively, and the 3rd cycle charging capacity was 148 mAh g^{-1}. Thus, the capacity retention of BaF_2-doped BiF_3 was seemingly improved compared to that of BiF_3 (Figure 1b), although the prolonged cycling performance of this material should be examined in future work. An important difference in the capacity retention of the two materials was found in the initial discharge–charge cycle. Moreover, the dQ dV^{-1} profiles of the $Bi_{0.8}Ba_{0.2}F_{2.8}$ electrode indicated that the initial discharging process was associated with an unique reaction (Figure S2).

Figure 2a shows the SR-XRD profiles of the $Bi_{0.8}Ba_{0.2}F_{2.8}$ electrode during the initial discharge–charge cycle. The $Bi_{0.8}Ba_{0.2}F_{2.8}$ powder prepared by mechanical milling had a tysonite (LaF_3)-type structure with the *P*–3*c*1 space group (Figure S3a), indicating that the Bi and Ba atoms randomly reside at the La site (6*f* in the Wycoff position) in the tysonite structure. The obtained lattice parameters were $a = 7.243$ Å and $c = 7.339$ Å. Based on a previous study [28], the lattice parameters of the tysonite-type BiF_3 (t-BiF_3) and $Bi_{0.8}Ba_{0.2}F_{2.8}$ should be $a = \sim 7.11$ Å and $c = \sim 7.30$ Å and $a = \sim 7.25$ Å and $c = \sim 7.33$ Å, respectively; the latter values are close to the ones obtained herein, indicating that the substitution of Bi^{3+} by Ba^{2+} with a larger ionic radius increases the lattice parameters. In the half- and fully discharged samples (#2 and #3), the diffraction peaks of the tysonite structure completely disappeared, suggesting the structure disruption during the early

stages of defluorination. Instead, broad peaks attributed to metallic Bi were observed (Figure S3b). No incorporation of Ba atoms was observed in metallic Bi. During the fluorination process (#4 and #5), the peaks of metallic Bi decreased in intensity, and a broad halo pattern characteristic of amorphous or nanocrystalline material was observed: the tysonite structure was not recovered. The SR-XRD profiles of the ball-milled BiF_3 electrode are shown in Figure S4 for comparison. We note that the prepared BiF_3 electrode had a cubic structure (c-BiF_3, Figure S4a). The t-BiF_3 phase is preferable to compare with $Bi_{0.8}Ba_{0.2}F_{2.8}$, but it is difficult to prepare pure t-BiF_3 to the best of our knowledge. Defluorination of c-BiF_3 produced metallic Bi (#3', Figure S4b). The diffraction peaks of the formed Bi were relatively sharp compared to those observed for the $Bi_{0.8}Ba_{0.2}F_{2.8}$ electrode, suggesting a larger crystallite size. The formation of c-BiF_3 was partly confirmed in the fully charged sample. This is qualitatively consistent with the large capacity loss observed in the initial discharge–charge profile (Figure S2). These results show that the detailed processes of the defluorination/fluorination reaction of c-BiF_3 and BaF_2-doped t-BiF_3 were slightly different from each other.

To understand the structure of the fluorinated material, reduced PDF analysis was performed (Figure 2b). The $S(Q)$ profiles were also shown in Figure S5. This method is powerful tool to characterize amorphous or nanocrystalline materials formed during electrochemical cycles [29–32]. The $G(r)$ function of the pristine sample (#1) corresponds to that of the tysonite structure. The interatomic distances related to the heavy metal Bi atom were primarily observed. A small peak at 2.5 Å is attributed to the nearest Bi-F pair, whereas the strong peaks at 4.3 and 7.3 Å correspond to the M-M (M = Bi and Ba) distances in the first and second coordination spheres. The $G(r)$ profile of the fully discharged $Bi_{0.8}Ba_{0.2}F_{2.8}$ sample (#3) resembles that of the fully discharged c-BiF_3 sample (#3', Figure S4c), corresponding to the metallic Bi profile. Due to the small amount of Ba atoms, the contribution of the Ba-containing material(s) could not be confirmed in $G(r)$. The

amplitude of the $G(r)$ profile of the fully charged sample (#5) disappeared above 25 Å, suggesting an amorphous or nanocrystalline character. This profile is relatively similar to that of pristine $Bi_{0.8}Ba_{0.2}F_{2.8}$ and more similar to the fully charged c-BiF_3 (#5', Figure S4c), indicating that the charged $Bi_{0.8}Ba_{0.2}F_{2.8}$ material is fluorinated. Especially, the first-neighbor M-M distance of the fully charged $Bi_{0.8}Ba_{0.2}F_{2.8}$ was close to that of c-BiF_3 rather than that of the pristine material (Figure S6). Therefore, the formation of a BiF_3-like local structure, instead of the original BaF_2-doped tysonite structure, is inferred in the fully charged $Bi_{0.8}Ba_{0.2}F_{2.8}$.

The Bi L_3-edge XAS spectra of the $Bi_{0.8}Ba_{0.2}F_{2.8}$ electrode samples are shown in Figure 3a. In the pristine sample (#1), the energy position of the absorption edge at $\mu(E) = 0.5$ coincides with o-BiF_3, indicating that the Bi valence state is Bi^{3+} in $Bi_{0.8}Ba_{0.2}F_{2.8}$. The absorption edge shifted to a lower energy by defluorination (#3), showing a reduction to metallic Bi [22]. In the fluorinated sample (#5), the absorption edge was almost the same as that of the pristine sample, which means that Bi^0 was reversibly oxidized to Bi^{3+}. Similar shifts of the absorption edge were also observed in the c-BiF_3 electrode (Figure S7). The energy at $\mu(E) = 0.5$ for the fully charged sample (#5') was lower than that for the pristine sample (#1'), suggesting the incomplete conversion from metallic Bi to c-BiF_3, as mentioned above. Figure 3b shows the Ba L_3-edge XAS spectra of the $Bi_{0.8}Ba_{0.2}F_{2.8}$ samples. The peak positions of the pristine (#1), fully discharged (#3), and fully charged samples (#5) were almost the same as that of BaF_2, indicating that the Ba valence is Ba^{2+} and is retained during the discharge–charge process [25]. Therefore, the Ba^{2+} ions randomly substituted the Bi^{3+} ions in the pristine $Bi_{0.8}Ba_{0.2}F_{2.8}$ tysonite structure, and only the Bi atom is a redox-active element during the discharge–charge process.

Figure 4a shows the bright-field (BF)-STEM image of the pristine electrode sample. The primary particle size of the ball-milled $Bi_{0.8}Ba_{0.2}F_{2.8}$ was estimated to be 6–8 nm in diameter. EDS

elemental mapping showed a similar distribution of Bi, Ba, and F atoms (Figure 4b–e). Nanobeam ED profiles matched the tysonite structure (Figure S8). EELS-STEM images of the fully discharged electrode are shown in Figure 5, where the high-angle annular dark-field (HAADF) image shows an accumulation of particles larger than 10 nm in diameter. On the one hand, elemental mapping shows a similar distribution of Ba and F atoms, which can be considered as BaF_2 (Figure 5c,d). On the other hand, the Bi atom shows a different distribution and is considered a metal (Figure 5e). The nanobeam ED profiles confirmed crystalline BaF_2 and metallic Bi (Figures S9 and S10). These particles seem to exist next to each other. Figure 6 shows the EELS-STEM images of the fully charged sample, where the Ba and Bi distributions are different (Figure 6d,e). The F distribution overlaps with the Ba and Bi distributions (Figure 6c). The nanobeam ED showed crystalline BaF_2 (Figure S11), suggesting that fluorination forms BiF_3 and does not form a Bi-Ba-F material.

The above results show that the tysonite structure decomposes into metallic Bi and nanocrystalline BaF_2 by defluorination and that metallic Bi then converts into amorphous or nanocrystalline BiF_3 by fluorination. In subsequent cycles, the conversion reaction between BiF_3 and Bi is expected to occur, leaving BaF_2 inactive. The metallic Bi formed by the defluorination of $Bi_{0.8}Ba_{0.2}F_{2.8}$ is considered to be a smaller particle than that formed by the defluorination of BiF_3, as demonstrated by the XRD profiles (Figures 2a and S4b). Therefore, we speculate that the cycle performance of the $Bi_{0.8}Ba_{0.2}F_{2.8}$ electrode would be improved compared to the BiF_3 electrode due to the suppression of the coarsening of BiF_3 particles by the adhesion of BaF_2 particles formed after initial defluorination.

4. Conclusions

In this study, we investigated the defluorination/fluorination reaction of a BaF_2-doped BiF_3, $Bi_{0.8}Ba_{0.2}F_{2.8}$, positive electrode. The $Bi_{0.8}Ba_{0.2}F_{2.8}$ electrode showed a higher reversible capacity

in the first cycle and improved capacity retention compared to the BiF_3 electrode. The XRD profile showed that $Bi_{0.8}Ba_{0.2}F_{2.8}$ prepared by mechanical alloying had a single phase of tysonite structure, where Bi and Ba atoms randomly enter in the same atomic position. A low-crystalline metallic Bi was observed in the discharged sample, indicating that the tysonite structure decomposed into Bi and BaF_2 nanoparticles during the defluorination process, as visualized in the HAADF-STEM images. The PDF and EELS analyses suggested the formation of BiF_3 nanoparticles in the charged sample. The XAS spectra at the Bi and Ba L_3-edge clearly indicate that bismuth is the only redox-active element. Therefore, we consider that the improved capacity retention of $Bi_{0.8}Ba_{0.2}F_{2.8}$ compared to BiF_3 may be due to the suppression of the coarsening of BiF_3 nanoparticles by the adhesion of BaF_2 nanoparticles formed after initial defluorination. The dispersed BaF_2 nanoparticles serve as mitigating the capacity degradation during cycles, whereas the coarsening proceeds in the undoped BiF_3 electrode causing larger degradation. This study suggests that controlling the by-product nanoparticle decomposed from a multicomponent fluoride is a simple technique to design a posteriori nanocomposite electrode with good cycle performance. The preparation of a single phase of multicomponent fluoride is an important first step for the purpose.

Acknowledgments

This work is based on results obtained from a project, “Research and Development Initiative for Scientific Innovation of New Generation Batteries (RISING and RISING2)”, JPNP09012 and JPNP16001, commissioned by the New Energy and Industrial Technology Development Organization (NEDO). The SR-XRD measurements were performed with the approval of the Japan Synchrotron Radiation Research Institute (JASRI, Proposal No. 2019A1148). The XAS measurements were performed with the approval of JASRI and RIKEN SPring-8 Center.

Appendix A. Supplementary data

Supplementary data related to this article can be found online at http://****.

References

[1] C. Rongeat, M.A. Reddy, T. Diemant, R.J. Behm, M. Fichtner, Development of new anode composite materials for fluoride ion batteries, J. Mater. Chem. A 2 (2014) 20861–20872.

[2] M.A. Reddy, M. Fichtner, Chapter 3 - Fluoride cathodes for secondary batteries, In Advanced fluoride-based materials for energy conversion, T. Nakajima, H. Groult, Eds. Elsevier (2015) 51–76.

[3] F. Gschwind, G. Rodriguez-Garcia, D.J.S. Sandbeck, A. Gross, M. Weil, M. Fichtner, N. Hörmann, Fluoride ion batteries: Theoretical performance, safety, toxicity, and a combinatorial screening of new electrodes, J. Fluor. Chem. 182 (2016) 76–90.

[4] X. Zhao, Z. Zhao-Karger, M. Fichtner, X. Shen, Halide-based materials and chemistry for rechargeable batteries, Angew. Chem. Int. Ed. 59 (2020) 5902–5949.

[5] G. Karkera, M.A. Reddy, M. Fichtner, Recent developments and future perspectives of anion batteries, J. Power Sources 481 (2021) 228877.

[6] J. Haruyama, K. Okazaki, Y. Morita, H. Nakamoto, E. Matsubara, T. Ikeshoji, M. Otani, Two-phase reaction mechanism for fluorination and defluorination in fluoride-shuttle batteries: A first-principles study, ACS Appl. Mater. Interfaces 12 (2020) 428–435.

[7] M.A. Reddy, M. Fichtner, Batteries based on fluoride shuttle, J. Mater. Chem. 21 (2011) 17059–17062.

[8] L.N. Patro, K. Hariharan, Fast fluoride ion conducting materials in solid state ionics: An overview, Solid State Ion. 239 (2013) 41–49.

[9] I. Mohammad, R. Witter, M. Fichtner, M.A. Reddy, Room-temperature, rechargeable solid-state fluoride-ion batteries, ACS Appl. Energy Mater. 1 (2018) 4766–4775.

[10] K. Okazaki, Y. Uchimoto, T. Abe, Z. Ogumi, Charge–discharge behavior of bismuth in a liquid electrolyte for rechargeable batteries based on a fluoride shuttle, ACS Energy Lett. 2 (2017)

1460–1464.

[11] R. Hagiwara, T. Hirashige, T. Tsuda, Y. Ito, A highly conductive room temperature molten fluoride: EMIF·2.3HF, J. Electrochem. Soc. 149 (2002) D1–D6.

[12] T. Yamamoto, K. Matsumoto, R. Hagiwara, T. Nohira, Room-temperature fluoride shuttle batteries based on a fluorohydrogenate ionic liquid electrolyte, ACS Appl. Energy Mater. 2 (2019) 6153–6157.

[13] V.K. Davis, C.M. Bates, K. Omichi, B.M. Savoie, N. Momcilovic, Q. Xu, W.J. Wolf, M.A. Webb, K.J. Billings, N.H. Chou, S. Alayoglu, R.K. McKenney, I.M. Darolles, N.G. Nair, A. Hightower, D. Rosenberg, M. Ahmed, C.J. Brooks, T.F. Miller III, R.H. Grubbs, S.C. Jones, Room-temperature cycling of metal fluoride electrodes: Liquid electrolytes for high-energy fluoride ion cells, Science 362 (2018) 1144–1148.

[14] H. Konishi, T. Minato, T. Abe, Z. Ogumi, Electrochemical performance of a bismuth fluoride electrode in a reserve-type fluoride shuttle battery, J. Electrochem. Soc. 164 (2017) A3702–A3708.

[15] H. Konishi, T. Minato, T. Abe, Z. Ogumi, Improvement of cycling performance in bismuth fluoride electrodes by controlling electrolyte composition in fluoride shuttle batteries, J. Appl. Electrochem. 48 (2018) 1205–1211.

[16] H. Konishi, T. Minato, T. Abe, Z. Ogumi, Triphenylboroxine and triphenylborane as anion acceptors for electrolyte in fluoride shuttle batteries, Chem. Lett. 47 (2018) 1346–1349.

[17] H. Konishi, T. Minato, T. Abe, Z. Ogumi, Influence of electrolyte composition on the electrochemical reaction mechanism of bismuth fluoride electrode in fluoride shuttle battery, J. Phys. Chem. C 123 (2019) 10246–10252.

[18] A. Celik-Kucuk, T. Yamanaka, T. Abe, Using siloxane-based liquid electrolytes with high stability for fluoride shuttle batteries, J. Mater. Chem. A 8 (2020) 22134–22142.

[19] T. Yamanaka, K. Okazaki, T. Abe, K. Nishio, Z. Ogumi, Evolution of reactions of a fluoride shuttle battery at the surfaces of BiF_3 microclusters studied by in situ Raman microscopy, ChemSusChem 12 (2019) 527–534.

[20] T. Yamanaka, T. Abe, K. Nishio, Z. Ogumi, In situ observation of fluoride shuttle battery reactions with dissolution-deposition mechanisms by Raman microscopy, J. Electrochem. Soc. 166 (2019) A635–A640.

[21] T. Yamanaka, A. Celik-Kucuk, Z. Ogumi, T. Abe, Evolution of fluoride shuttle battery reactions of BiF_3 microparticles in a CsF/LiBOB/tetraglyme electrolyte: Dependence on structure, size, and shape, ACS Appl. Energy Mater. 3 (2020) 9390–9400.

[22] H. Konishi, A. Celik-Kucuk, T. Minato, T. Abe, Z. Ogumi, Improved electrochemical performances in a bismuth fluoride electrode prepared using a high energy ball mill with carbon for fluoride shuttle batteries, J. Electroanal. Chem. 839 (2019) 173–176.

[23] A. Rhandour, J.M. Reau, S.F. Matar, S.B. Tian, P. Hagenmuller, New fluorine ion conductors with tysonite-type structure, Mater. Res. Bull. 20 (1985) 1309–1327.

[24] H. Konishi, T. Minato, T. Abe, Z. Ogumi, Electrochemical reaction mechanism for $Bi_{1-x}Ba_xF_{3-x}$ (x = 0, 0.1, 0.2, and 0.4) electrodes in lithium-ion batteries, ChemistrySelect 2 (2017) 6399–6406.

[25] H. Konishi, T. Minato, T. Abe, Z. Ogumi, Electrochemical performance of BiF_3-BaF_2 solid solution with three different phases on a fluoride shuttle battery system, ChemistrySelect 5 (2020) 4943–4946.

[26] S. Kohara, M. Itou, K. Suzuya, Y. Inamura, Y. Sakurai, Y. Ohishi, M. Takata, Structural studies of disordered materials using high-energy x-ray diffraction from ambient to extreme conditions, J. Phys.: Condens. Matter 19 (2007) 506101.

[27] B. Ravel, M. Newville, ATHENA, ARTEMIS, HEPHAESTUS: Data analysis for X-ray

absorption spectroscopy using IFEFFIT, J. Synchrotron Radiat. 12 (2005) 537–541.

[28] J.M. Reau, S.B. Tian, A. Rhandour, S. Matar, P. Hagenmuller, Respective influence of optimization criteria on transport properties of $Ba_{1-x}M'_xF_{2+x}$ solid solution (M' = In, Bi), Solid State Ion. 15 (1985) 217–223.

[29] B. Key, M. Morcrette, J.-M. Tarascon, C.P. Grey, Pair distribution function analysis and solid state NMR studies of silicon electrodes for lithium ion batteries: Understanding the (de)lithiation mechanism, J. Am. Chem. Soc. 133 (2011) 503–512.

[30] F. Wang, R. Robert, N.A. Chernova, N. Pereira, F. Omenya, F. Badway, X. Hua, M. Ruotolo, R. Zhang, L. Wu, V. Volkov, D. Su, B. Key, M.S. Whittingham, C.P. Grey, G.G. Amatucci, Y. Zhu, J. Graetz, Conversion reaction mechanisms in lithium ion batteries: Study of the binary metal fluoride electrodes, J. Am. Chem. Soc. 133 (2011) 18828–18836.

[31] A. Grenier, A.-G. Porras-Gutierrez, H. Groult, K.A. Beyer, O.J. Borkiewicz, K.W. Chapman, D. Dambournet, Electrochemical reactions in fluoride-ion batteries: Mechanistic insights from pair distribution function analysis, J. Mater. Chem. A 5 (2017) 15700–15705.

[32] K. Ohara, S. Tominaka, H. Yamada, M. Takahashi, H. Yamaguchi, F. Utsuno, T. Umeki, A. Yao, K. Nakada, M. Takemoto, S. Hiroi, N. Tsuji, T. Wakihara, Time-resolved pair distribution function analysis of disordered materials on beamlines BL04B2 and BL08W at SPring-8, J. Synchrotron Radiat. 25 (2018) 1627–1633.

Figures and Figure captions

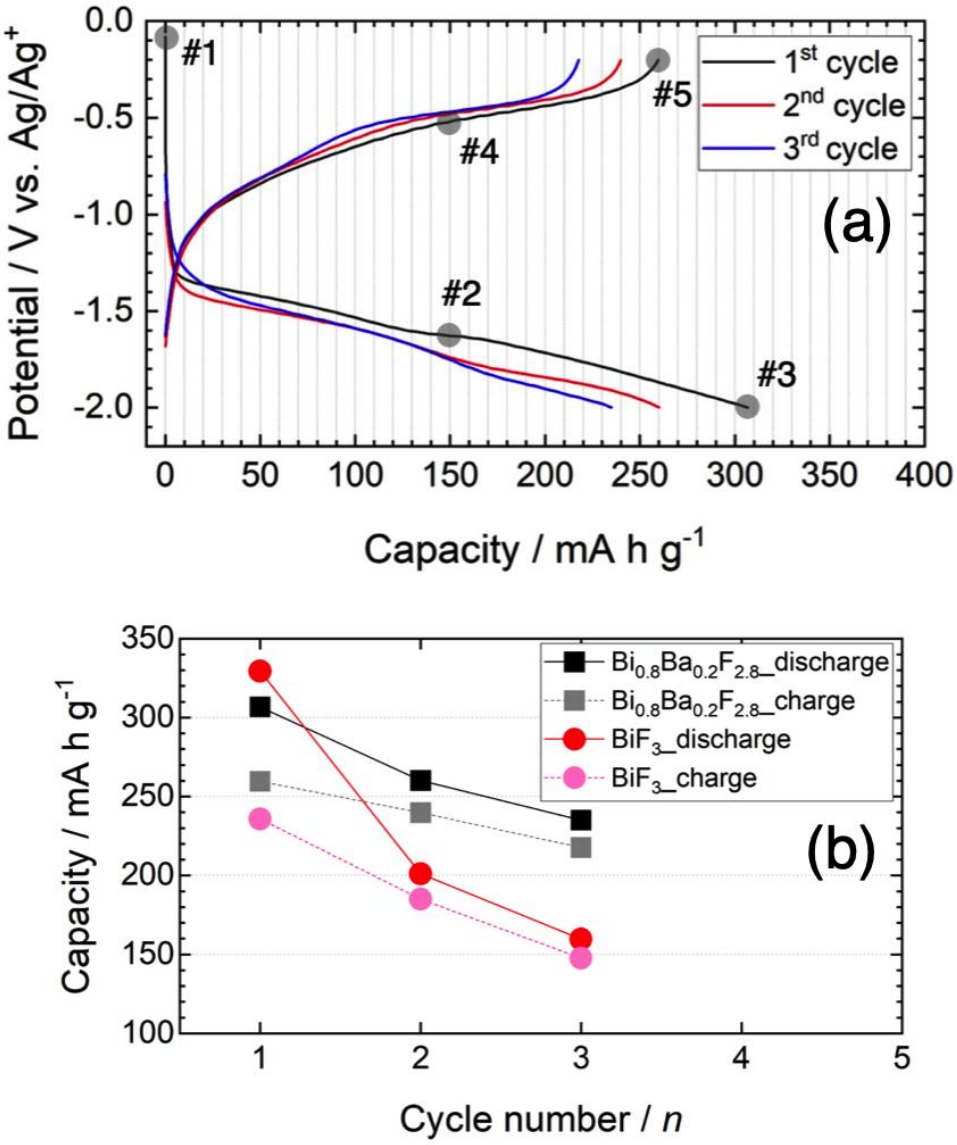

Fig. 1. (a) Discharge–charge profiles of the $Bi_{0.8}Ba_{0.2}F_{2.8}$ electrode. The sampling points were marked. (b) Comparison between the discharging and charging capacities of $Bi_{0.8}Ba_{0.2}F_{2.8}$ and c-BiF_3.

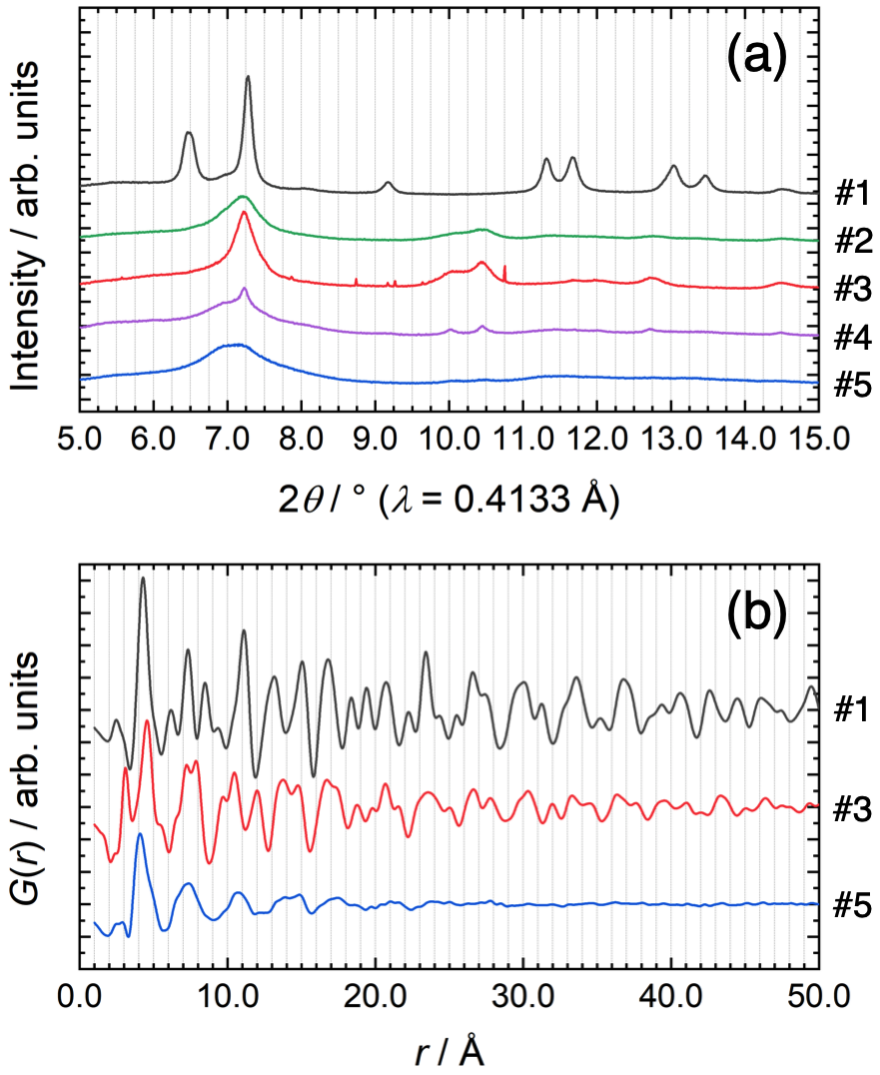

Fig. 2. (a) XRD and (b) reduced PDF, $G(r)$, profiles of the $Bi_{0.8}Ba_{0.2}F_{2.8}$ electrode during the initial discharge–charge cycle. The sample numbers are described in Figure 1a.

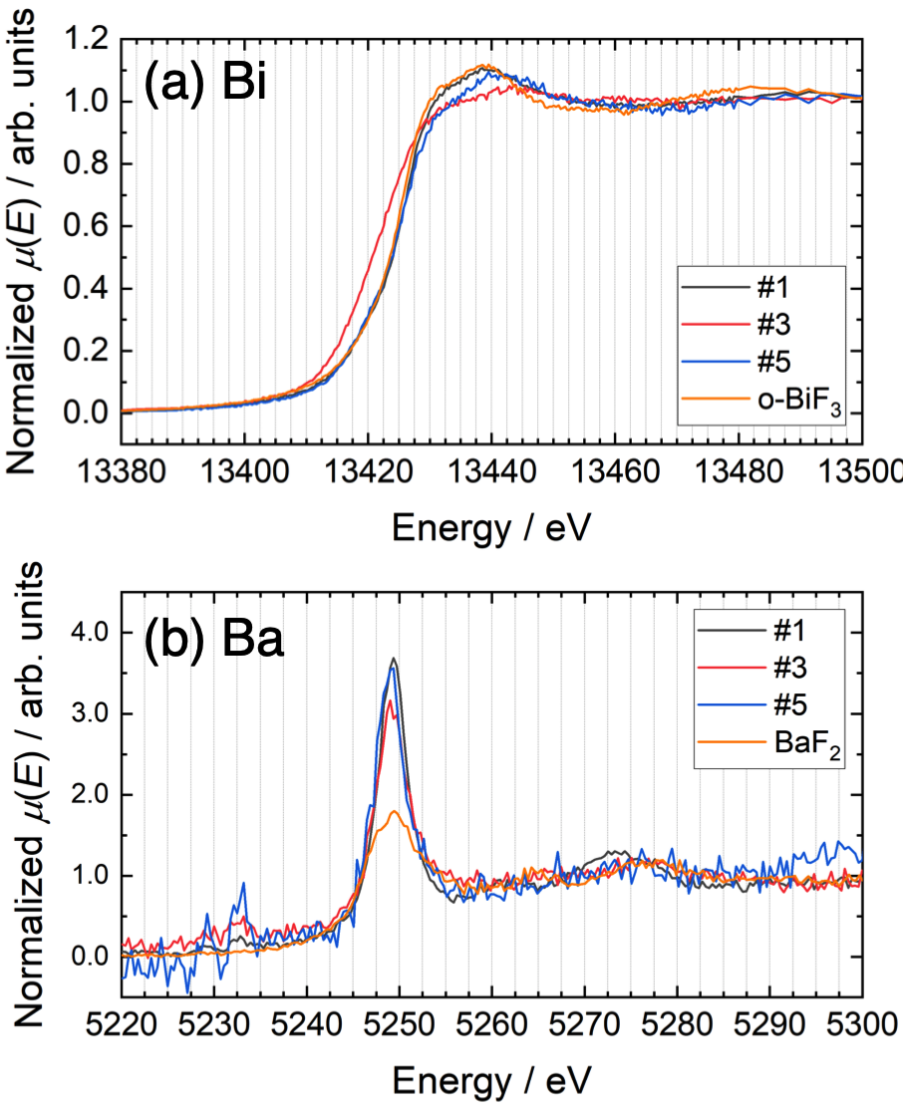

Fig. 3. (a) Bi and (b) Ba L_3-edge XAS spectra of the $Bi_{0.8}Ba_{0.2}F_{2.8}$ electrode during the initial discharge–charge cycle. The sample numbers are described in Figure 1a.

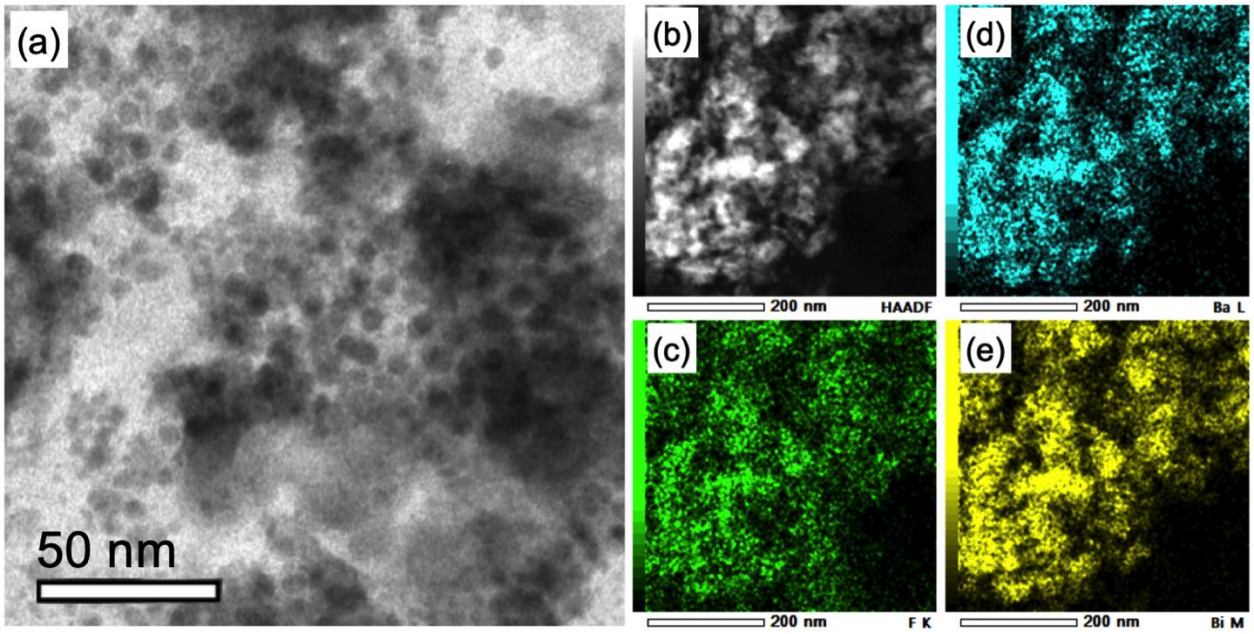

Fig. 4. (a) BF-STEM and (b–e) EDS mapping images of the pristine $Bi_{0.8}Ba_{0.2}F_{2.8}$ electrode. (b) HAADF image, (c) F *K*-edge, (d) Ba *L*-edge, and (e) Bi *M*-edge maps.

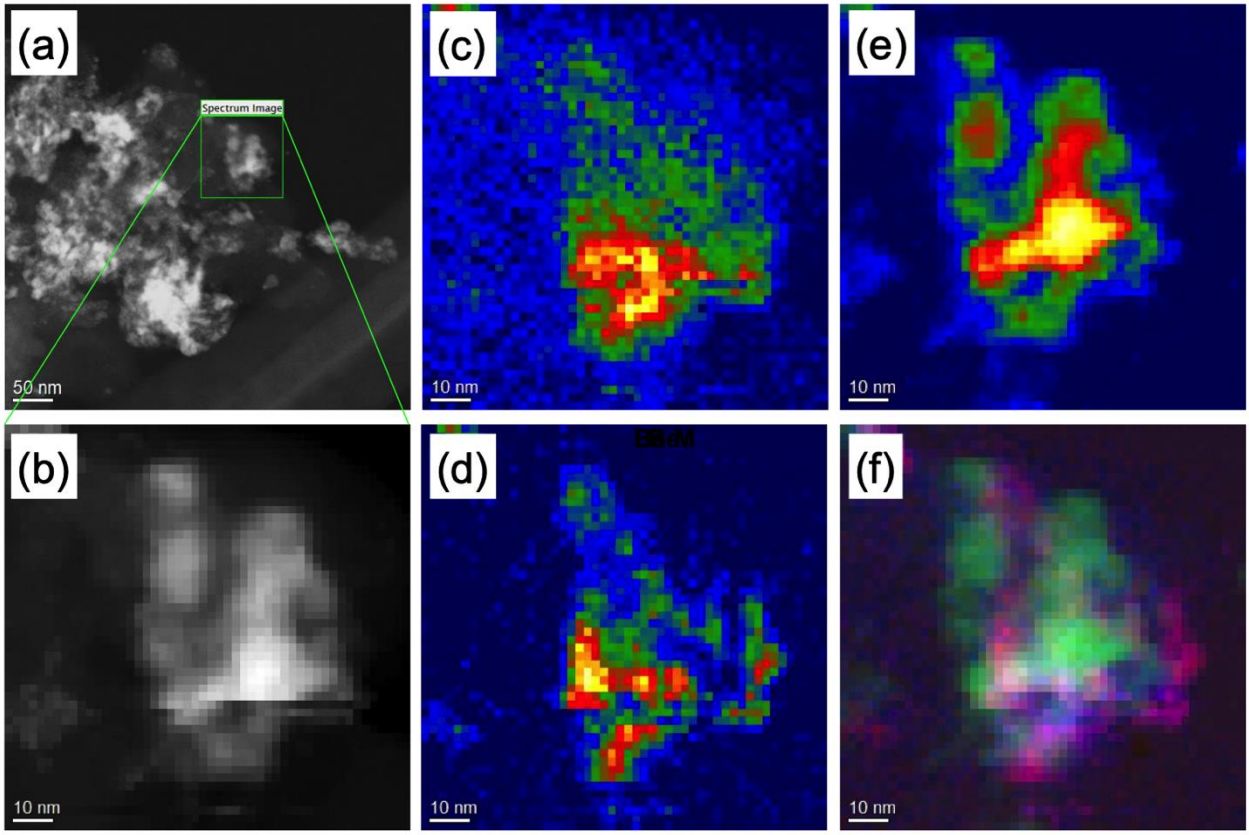

Fig. 5. EELS mapping images of the $Bi_{0.8}Ba_{0.2}F_{2.8}$ electrode disassembled in the fully discharged state. (a,b) HAADF images, (c) F *K*-edge, (d) Ba *M*-edge, (e) Bi *M*-edge maps, and (f) overlapped images of F (blue), Ba (magenta), and Bi (green).

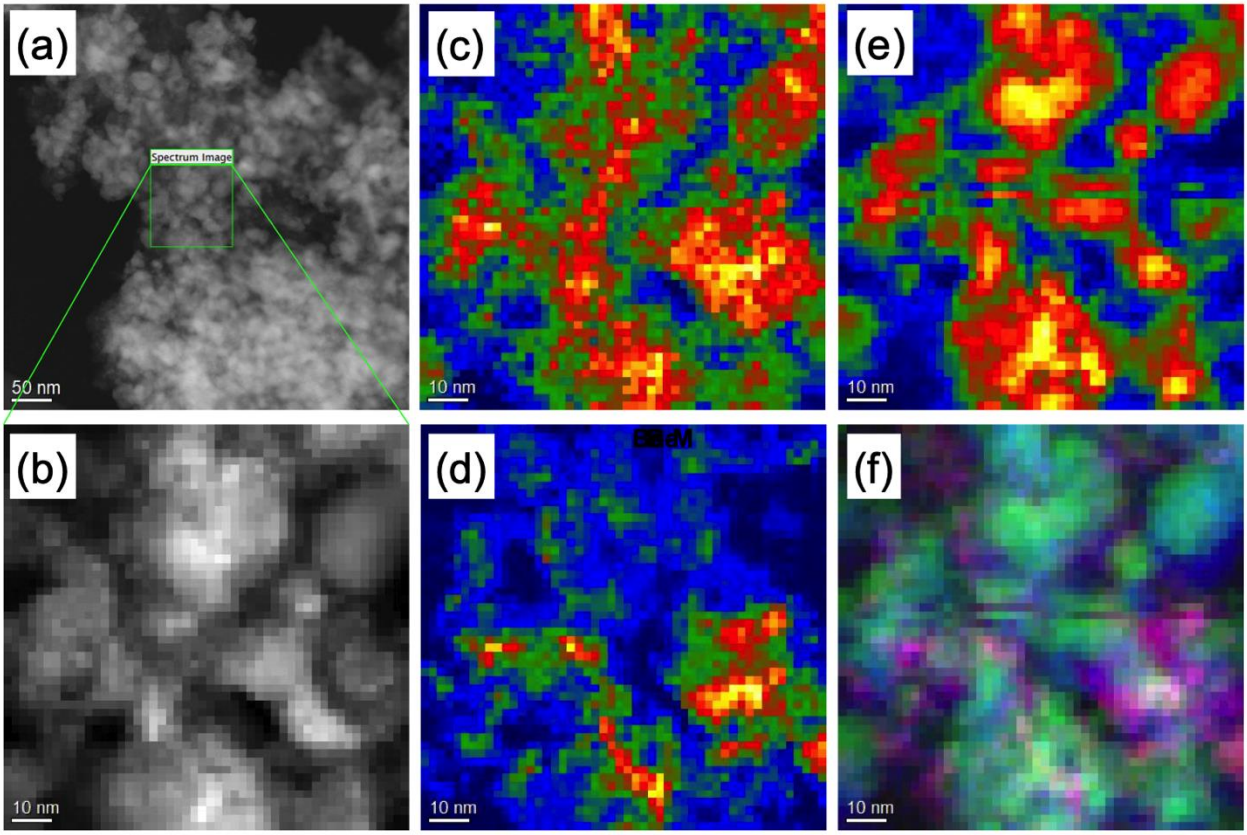

Fig. 6. EELS mapping images of the $Bi_{0.8}Ba_{0.2}F_{2.8}$ electrode disassembled in the fully charged state. (a,b) HAADF images, (c) F *K*-edge, (d) Ba *M*-edge, (e) Bi *M*-edge maps, and (f) overlapped images of F (blue), Ba (magenta), and Bi (green).